Chemical Science

Accepted Manuscript

This article can be cited before page numbers have been issued, to do this please use: J. Yang, S. Zhao, W. Huang, B. Chan, Z. Xu, M. Yin, W. Lin, M. Chai, R. Lin, S. Yu, M. Lu, N. Li, W. Li, X. Zhang, V. Chen and J. Hou, *Chem. Sci.*, 2026, DOI: 10.1039/D6SC00077K.

ROYAL SOCIETY OF CHEMISTRY

rsc.li/chemical-science

View Article Online
DOI: 10.1039/D6SC00077K

ARTICLE

Melt-Sintering of MOF Glass–2D Nanosheet Composites for Enhanced Processability and Gas Separation Performance

Received 00th January 20xx,
Accepted 00th January 20xx

DOI: 10.1039/x0xx00000x

Jie Yang, [a] Shuke Zhao, [a] Wengang Huang, [a] Bun Chan, [b] Zhonghao Xu, [c] Meilin Yin, [a] Weikang Lin, [d] Milton Chai, [a] Rijia Lin, [a] Shuwen Yu, [e] Mingyuan Lu, [d] Na Li, [*,f] Wei Li, [g] Xiwang Zhang, [c] Vicki Chen, [a] Jingwei Hou*[ac]

Amorphous metal-organic framework (MOF) glasses offer processible microporous materials for separation, sensing and catalysis, but their practical implementation has been limited by mechanical stability and ill-defined microporous structures. Here, we report a strategy to integrate g-C_3N_4 nanosheets into MOF glass via high-temperature sintering. Interfacial coupling, including π-π stacking and coordination-assisted bonding, effectively guide the packing of the nanosheets, improve structural integrity, and mitigate processing-induced stress during the MOF glass vitrification. By tuning the sintering temperature, the interlayer spacing of the g-C_3N_4 can be adjusted and stabilized, generating more regulated transport channels. The resulting hybrid glass can be processed into membranes, showing a two-order-of-magnitude increase in hydrogen permeance compared to pure MOF glass, with the selectivity for difference gas pairs also significantly improved. This contribution establishes a generalizable method for interlayer spacing engineering within hybrid glasses, demonstrating the incorporating of 2D materials can enhance the processability and separation performance on the composite glass.

Introduction

The ever growing demand for energy-efficient separation technologies has driven significant efforts towards developing advanced materials capable of selective gas transport[1]. Membrane-based separations, in particular, offer an easy-to-deploy, continuous, low-energy alternative to conventional thermally driven separation process such as distillation, absorption and adsorption[2]. Among different membrane material candidates, metal-organic frameworks (MOFs) have emerged as a versatile class of functional materials featuring tuneable pore structures, chemistry, enabling their exceptional molecular separation capability[3]. However, despite these advantages, the translation of MOF materials (most are crystalline phases) into macroscopic, processable, and mechanically robust membranes remains challenging[4]. The intrinsic brittleness of MOF crystals and the difficulty of forming continuous, pinhole-free layers often result in poor scalability and limited long-term stability[5,6]. Recently, the discovery of amorphous MOF glasses has opened new possibilities for overcoming these limitations[7,8]. These materials preserve the local coordination network of MOFs while exhibiting isotropic, continuous structures and thermoplastic processability[9–11], making them promising candidates for next-generation separation membranes.

Despite their promising processability, MOF glass materials still face intrinsic challenges in microstructure control[12] and mechanical reliability[13]. The loss of long-range order during the vitrification usually leads to broad pore size distribution with poorly defined gas transport pathways[14]. In addition, the amorphous framework normally processes high viscosity near their glass transition temperature[15–17], which restricts the relaxation of internal stress during cooling. The accumulated stress can generate cracks as the high temperature melt solidifies, significantly compromising the mechanical integrity of the MOF glass based thin films and membranes[18,19]. These defects further generate non-selective pathways that degrade gas separation performance. Therefore, although MOF glass is a promising and attractive candidate for defect fabrication given its balanced rigidity and processability, their limited mechanical resilience and uncontrolled microstructure remain key challenges to their implementation in molecular separation membranes[20,21].

Incorporating two-dimensional (2D) materials into glass substrate can be an effective method to tailor both mechanical and transport properties at the nanoscale[3,22]. The intrinsic mechanical robustness, chemical stability and tuneable interlayer space of 2D materials offer unique opportunities for reinforcing hybrid glasses and control their internal pore structures[23]. Among various candidates, graphitic carbon nitride (g-C_3N_4) has attracted growing attention due to its conjugated structure, rich functional groups and satisfactory chemical and

[a.] Nanomaterials Centre, School of Chemical Engineering, The University of Queensland, St Lucia, Queensland 4072, Australia
[b.] Graduate School of Engineering, Nagasaki University, Nagasaki 852-8521, Japan
[c.] ARC Centre of Excellence for Green Electrochemical Transformation of Carbon Dioxide, Brisbane, 4072 Australia
[d.] School of Mechanical and Mining Engineering, The University of Queensland, St Lucia, Queensland 4072, Australia
[e.] School of Chemistry and Chemical Engineering, Suzhou University, Suzhou, 234000, China
[f.] College of Chemistry, Nankai University, Tianjin 300071, China
[g.] School of Material Science and Engineering, Nankai University, Tianjin 300071, China
† Supplementary Information available: [details of any supplementary information available should be included here]. See DOI: 10.1039/x0xx00000x

thermal stability[24]. When incorporated into a substrate, g-C_3N_4 can act as a stable scaffold that constrains local structural variation of the composite[25]. In addition, its periodic nanosheet structure allows regulation of the interfacial interactions and free space within the composite, potentially provide molecular transport pathways for fine-tuning gas separation[26]. However, controlling and stabilising the interlayer spacing of g-C_3N_4 remains challenging, as the layers are held together mainly by weak van der Waals forces that tend to fail or reorganise under thermal, solvent or mechanical conditions[27,28].

In this work, we introduce a strategy to address the intrinsic mechanical fragility and poorly defined pore structure of MOF glass by integrating layered 2D g-C_3N_4 into the glass matrix. Through a combination of structure, thermal and chemical structure analysis, we revealed that g-C_3N_4 promotes local interfacial coupling with the MOF glass matrix, which helps regulate glass densification and partially relieve processing-induced stress during vitrification. In addition, the interlayer spacing of g-C_3N_4 within the composite can be readily tuned by adjusting the sintering temperature and its loading, enabling fine tuning of the microstructure and gas transport channels. This composite modulation leads to an enhancement of the composite's processibility, mechanical structure and separation capability. As demonstrated in our gas separation tests, the composite membrane demonstrated an extraordinary two-order-of-magnitude increase in hydrogen permeance compared to the pure MOF glass, along with a substantial improvement in H_2/CO_2 selectivity from 7 to 21. These discoveries underscore the potential of this composite approach for developing robust and high-performing membranes and thin films.

Results and Discussions

ZIF-62 crystals were synthesized via a solvothermal method by dissolving $Zn(NO_3)_2$ and mixed ligands (benzimidazole, bIm, and imidazole, Im) in DMF, followed by 120 °C treatment. The crystalline structure was confirmed by powder X-ray diffraction (PXRD) (Fig. S1). The molar ratio of the linkers (bIm/Im = 1.75/0.25) in the crystalline phase was determined using ^{1}H liquid nuclear magnetic resonance spectroscopy (NMR) (Fig. S2). g-C_3N_4 was prepared via a convenient top-down approach, wherein melamine was thermally sintered slowly in air to facilitate self-assembly into a two-dimensional lamellar structure showing in the SEM (Fig. S3). The obtained ZIF-62 crystals and g-C_3N_4 powders were mixed in isopropanol according to a predetermined mass ratio, ground into a homogeneous viscous slurry (denoted as ZIF-62_CN-x, where *x* represents the mass fraction of g-C_3N_4), and then pressed into pellets. The pellets were then thermally treated under an argon atmosphere and held at the target temperature for 30 min, followed by melt-quenching to room temperature to obtain self-supporting, in situ-formed glassy composites.

For the pure ZIF-62, it exhibits representative MOF glass formation behaviour. The transformation from crystalline ZIF-62 to its amorphous glass form (denoted as a_gZIF-62, where "a_g" stands for amorphous glass) was achieved by heating the crystals above their melting point (T_m = 440 °C), as determined from the first upscan of differential scanning calorimetry (DSC) result in Fig. S4, followed by quenching to room temperature. After quenching, the Bragg diffraction peaks of crystalline ZIF-62 disappeared in XRD, replaced by a diffuse scattering at ca. 16°, confirming the formation of a_gZIF-62 glassy phase. A comparable tendency can be seen in Fig. 1b in which the melting point of ZIF-62_CN-25 composite occurs at 448 °C during the first upscan, and the emergence of a glass transition behaviour appears at 332 °C in the second DSC upscan. The thermal behavior of ZIF-62_CN-10 and ZIF-62_CN-40 composites during melting was further studied through combined mass reduction in thermogravimetric (TG) and DSC analyses. The endothermic peak observed between 150 °C and 250 °C in the first DSC upscan corresponds to the mass loss of residual solvent, i.e. DMF, retained in the ZIF-62 pores (Fig. S4), as corroborated by the mass loss observed in the TG curve ca. 150-250 °C (Fig. S4d). TG confirmed that both g-C_3N_4 and ZIF-62_CN were thermally stable up to 500 °C without noticeable decomposition (Fig. S4). A key observation from the first DSC upscan is that the melting temperature (T_m), identified as the second endothermic peak of the ZIF-62_CN composites, initially increased and then decreased with increasing g-C_3N_4 content, accompanied by progressive peak broadening. During the second heating ramp, ZIF-62_CN composites exhibited a glass transition temperature (T_g), a defining characteristic of amorphous glassy materials, confirming the successful transformation of ZIF-62 into the glassy state. This confirms that the incorporation of g-C_3N_4 does not compromise the thermal stability of ZIF-62 nor hinder its glass-forming ability. Furthermore, T_g of the ZIF-62_CN-x composites were found to be elevated compared to that of pure ZIF-62 (Fig. 1b, c), likely due to interfacial interactions that enhance the rigidity and connectivity of the hybrid network[29]. High-resolution synchrotron in-situ temperature variation X-ray powder diffraction (XRPD) further reveals the structural transformation during thermal processing of the ZIF-62_CN-25 composite (Fig. 1d). Upon heating, the diffraction peaks of crystalline ZIF-62 gradually diminish and ultimately vanish as it melts into an amorphous glass. Meanwhile, g-C_3N_4 exhibits the characteristic layered conjugated polymeric structure, where a prominent peak at ca. 27° attributed to the (002) plane associated with interlayer π-stacking of the tri-s-triazine aromatic frameworks[30]. This peak initially downshifts during the heating stage (400-450 °C), followed by an upshift during quenching, ultimately stabilizing at ca. 27.8°.

According to the in-situ powder diffraction results, the interlayer spacing of g-C_3N_4 exhibits a strong temperature dependence. The glass composite, including samples with different g-C_3N_4 loadings and treatment temperatures, were further examined by ex-situ PXRD to probe the variation of the interlayer distance. In this work, the composite glassy samples were denoted to as a_gZIF-62_CN-x. Taking the a_gZIF-62_CN-25 composite as an example, ex-situ PXRD patterns in Fig. 1e exhibit a trend of upward shifting by approximately ca. 0.2° with higher sintering temperature, indicating the glassy composite

View Article Online
DOI: 10.1039/D6SC00077K

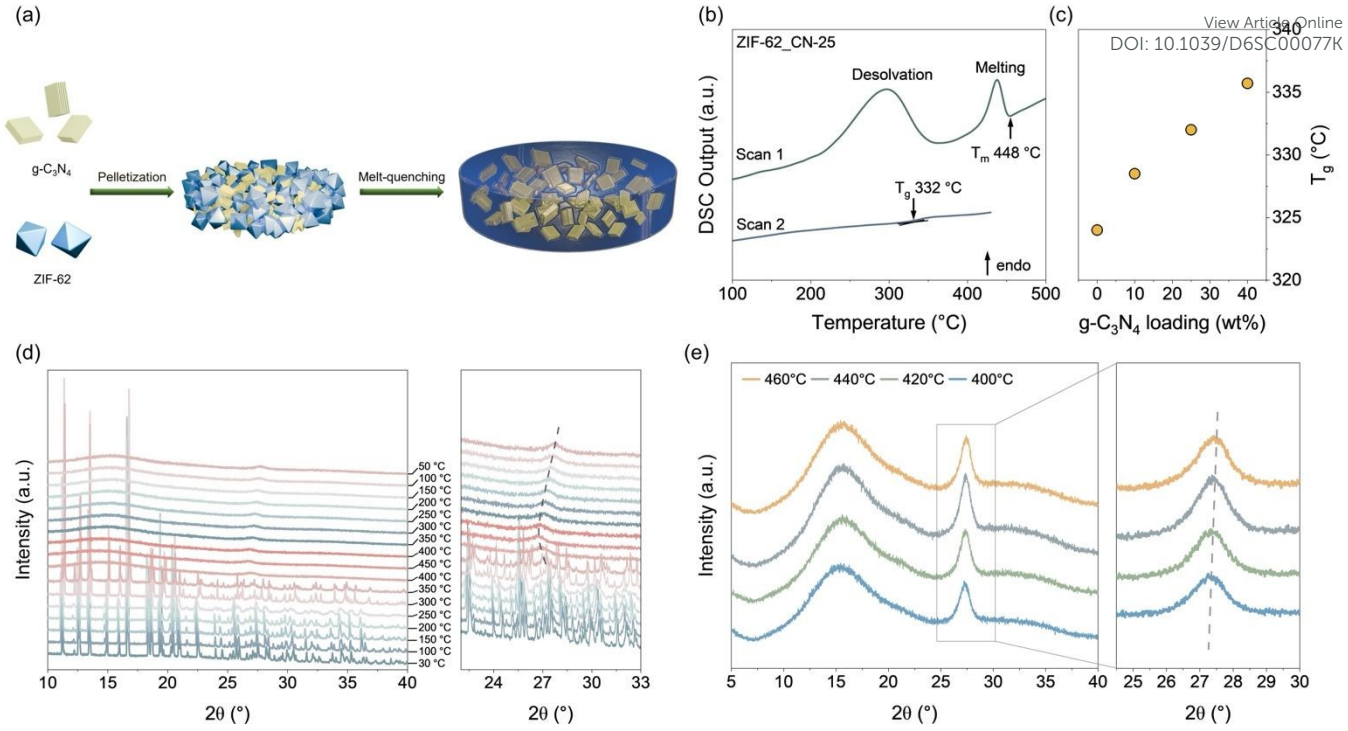

Fig. 1 Transformation of crystalline structure and thermal behavior of synthesized glass composite (a) Fabrication of glass composite pellet. (b) DSC analysis for a_gZIF-62_CN-25 composite. (c) Glass transition temperatures of various glass composites. (d) Temperature variation Synchrotron radiation XRPD patterns of selected ZIF-62_CN-25 derivatives before and after heating to 450 °C (λ = 0.45920 Å). (e) XRD pattern of a_gZIF-62_CN-25 composite at 400 °C, 420 °C, 440 °C, 460 °C.

can stabilize the different interlayer distance even when being cooled back to the ambient temperature.

We further identified the interlayer distance can be readily tuned through different g-C_3N_4 loadings (Fig. 2a). Similar to pure a_gZIF-62, all composite samples exhibit a broad diffuse scattering peak, indicating the loss of long-range order and the formation of an amorphous phase. Compared with pristine g-C_3N_4, the diffraction peaks of g-C_3N_4 in a_gZIF-62_CN-x composites are preserved after melt-quenching at 440 °C, confirming the preservation of the g-C_3N_4 stacking structure. Notably, a constant up shift is observed in the a_gZIF-62_CN-10, a_gZIF-62_CN-25, a_gZIF-62_CN-40 composite, indicating a gradual contraction of the g-C_3N_4 materials. However, when the g-C_3N_4 loading reaches 50 wt%, this peak shift is no longer apparent when compared with the pristine g-C_3N_4. The observed shift of the g-C_3N_4 (002) reflection is closely linked to interfacial interactions within the composite. At moderate g-C_3N_4 loadings, the molten a_gZIF-62 phase effectively wets and confines g-C_3N_4 stacks during melt-quenching, producing strong interfacial confinement that contracts the interlayer spacing and shifts the (002) peak to higher angles. By contrast, at excessive g-C_3N_4 loadings, a larger fraction of g-C_3N_4 remains unconfined or undergoes aggregation/phase separation; the diffraction signal thus becomes dominated by these bulk-like domains and the net peak shift is diminished. Hence, the magnitude of the (002) peak shift reflects the extent of interfacial confinement afforded by the glass phase rather than the nominal g-C_3N_4 content alone.

To further validate the nanoscale structural change at the microscopic level, high-resolution transmission electron microscopy (HRTEM) was employed. As shown in Fig. S5 and Fig. 2b, the pristine g-C_3N_4 exhibits well-defined lattice fringes with an interlayer spacing of ca. 0.329 nm, corresponding to the (002) graphitic plane. In contrast, in the a_gZIF-62_CN-25 composite, the layered domains preserved within the amorphous glass matrix display a slightly contracted spacing of ca. 0.32 nm. The magnified view of the amorphous glass area (Fig. 2b1) confirms the absence of lattice ordering[31], while the confined g-C_3N_4 stacking regions (Fig. 2b2) and their corresponding FFT-assisted fringe fitting (Fig. 2b3) clearly reveal periodic fringes with reduced spacing. This nanoscale densification of g-C_3N_4 layers aligns with the PXRD peak upshift, collectively indicating that the ZIF-62 glass matrix imposes interlayer confinement and enhances g-C_3N_4 stacking compactness during vitrification. The microstructural observations further corroborate this interfacial confinement, as the TEM images reveal intimate contact between the glass and g-C_3N_4 phases without discernible interfacial voids or defects.

View Article Online
DOI: 10.1039/D6SC00077K

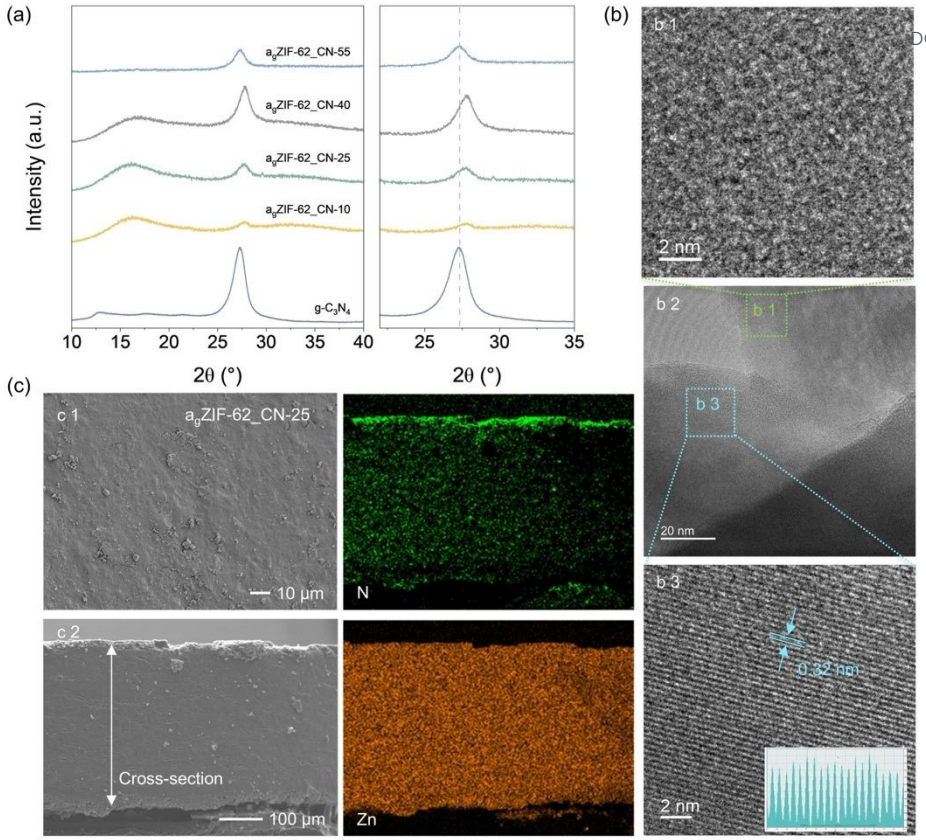

Fig. 2 Morphology and interlayer structure of glass composites (a) XRD patten of a_gZIF-62_CN-x composites and pure g-C_3N_4. (b1-b3) High-resolution TEM image of a_gZIF-62_CN-25 composite. and its line profile analysis extracted from the HRTEM image, illustrating the periodic contrast with apparent spacing. (c) SEM surface and cross-sectional images of a_gZIF-62_CN-25 glass composite pellet with the Zn and N elemental distribution.

To evaluate the microstructural integrity of the composites, scanning electron microscopy (SEM) was employed to examine the surface and cross-sectional morphologies before and after melting (Fig. 2c, Fig. S6, 7). The thickness of the self-supporting a_gZIF-62_CN-25 membrane was determined from the cross-sectional SEM image to be approximately 367 µm (Fig. S7). The loos, two-dimensional g-C_3N_4 can be readily embedded and dispersed within the molten ZIF-62 phase, in contrast to crystalline fillers with distinct grains. The cross-section also reveal a dense, void-free structure compared with the pre-melted samples, confirming that the two distinct phases are intimately integrated. In addition, satisfactory interfacial compatibility ensures structural uniformity and homogeneity, as further verified by the SEM-EDS elemental mapping.

To further elucidate the chemical environment changes and interfacial interactions, synchrotron X-ray absorption spectroscopy was employed to probe the local environment of Zn atoms for the composite. The X-ray absorption near-edge structure (XANES) spectra revealed distinct intensity differences between the ZIF-62_CN-25 crystalline composite and the a_gZIF-62_CN-25 glass composite (Fig. 3a). In particular, the feature at ~9673 eV decreased in intensity, while the peak at ~9667 eV became slightly more pronounced in the glass composite. These spectral variations indicate modifications in the local electronic environment and coordination symmetry of Zn[32], consistent with a slight reduction in the average coordination number. To further resolve the coordination shells, extended X-ray absorption fine structure (EXAFS) analysis (Fig. 3b) combined with wavelet transform (WT) mapping was performed (Fig. 3c, d and Fig. S8). Both methods confirmed differences in bond distances and coordination numbers (Table S1), with the glass composite showing an additional weak contribution from Zn-Zn atom pairs. The weak Zn-Zn contribution at ca. 2.5 Å with a low coordination number indicates that a small fraction of Zn sites undergo local rearrangement during melt-quenching, although minor thermally induced local decomposition cannot be fully excluded. This interpretation is consistent with the additional DFT cluster models, which suggest a locally off-centered and distorted Zn coordination environment near the g-C_3N_4 interface. These results demonstrate that vitrification preserves the Zn-N tetrahedral framework while introducing weak but detectable Zn-Zn correlations, which likely reflect partial inter-tetrahedral proximity induced by structural rearrangements and interfacial confinement during melt-quenching[33].

The collective framework motion of localized environments in glass composite materials is exposed by terahertz (THz) /far-infrared (FarIR) spectroscopy. Compared to a_gZIF-62 and pristine g-C_3N_4 (Fig. S9), glass composite materials with different loadings exhibit two key structural changes in Fig. S10. Firstly, in the low-frequency region, a bond around 300 cm^{-1}

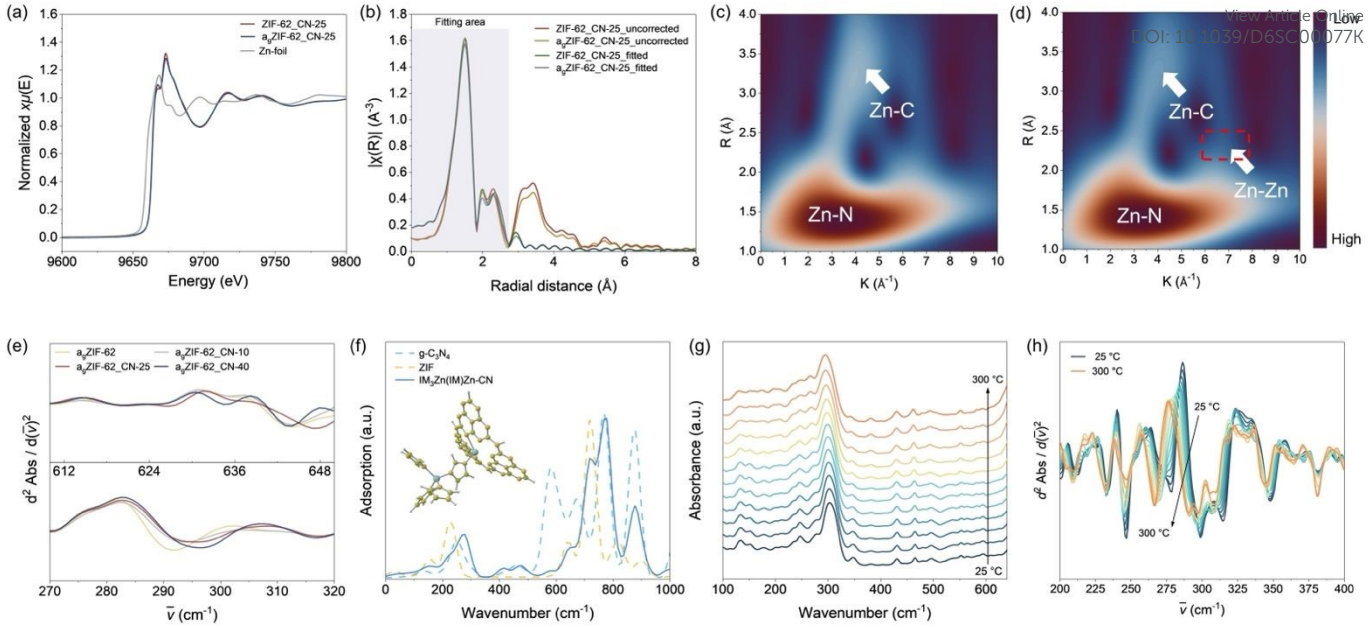

Fig. 3 Characterizations of chemical environment of the composites. (a) Normalized Zn K-edge XANES spectra of ZIF-62_CN-25 and a_gZIF-62_CN-25. (b) X-ray absorption fine structure (EXAFS) Fourier transform magnitude spectrum of ZIF-62_CN-25 and a_gZIF-62_CN-25. (c, d) Full-range wavelet transform (WT) representation for the Zn K edge of (c) ZIF-62_CN-25 composite and (d) a_gZIF-62_CN-25 glass composite. (e) Second derivative spectra corresponding to 270-320 cm^{-1} and 610-650 cm^{-1} ex-situ THz/FarIR of a_gZIF-62 and a_gZIF-62_CN-x composite. (f) DFT calculated $IM_3Zn(IM)Zn$-CN tetrahedron spectra in the wavenumber range to 1000 cm^{-1}, with the schematic diagram of the corresponding vibrational movements for DFT calculation at 298 K. Zn, blue; C, green; N, orange; and H, white. (g) In-situ THz/FarIR spectra for ZIF-62_CN-25 up to 573 K. (h) Second derivative spectra corresponding to subtle changes of (g) in-situ THz/FarIR spectra.

shifts toward higher wavenumbers in the glass composite relative to pure a_gZIF-62 (Fig. 3e, S10), which is attributed to Zn-centered framework deformation within Zn tetrahedra. Secondly, a small hump appears near 630 cm^{-1} in the composite, more clearly visible in the second derivative analysis shown in the Fig. 3 (e), is consistent with the deformation behavior of the aromatic ring within the structure.

To reveal the mechanism of structural deformation and interfacial interactions of glass composite materials, we carried out simulations by density functional theory (DFT). The coordination environments between Zn and Lewis basic functions of g-C_3N_4 structure give rise to the bond variation for glass composite materials. Specifically, when Zn interacts with N sites of g-C_3N_4, partial interactions between ZIF and g-C_3N_4 ($IM_3Zn(IM)ZnIM$–CN) happen (Fig. S11), leading to a slight shift of the band to ~260 cm^{-1} band, whereas complete accommodation of Zn in the in-plane intrinsic g-C_3N_4 pores ($IM_3Zn(IM)Zn$–CN) resulted in a steric deformation with a result of more pronounced shift to ~280 cm^{-1} and the appearance of a new feature, which is in qualitative agreement with the experimental observations (Fig. 3f). Additional DFT cluster models (Fig. S22) with increased structural size suggest that Zn becomes locally off-centered near the g-C_3N_4 interface, giving rise to a broader distribution of Zn-N distances (Table. S3). Mode analysis indicates that stronger interfacial coupling enhances Zn-centered framework deformations and mixes them with low-frequency motions of the g-C_3N_4 scaffold. It should be noted that these finite DFT cluster models are used to probe local Zn coordination geometry and short-range vibrational features, rather than to fully reproduce long-wavelength collective phonon modes in the bulk glass. Temperature-resolved synchrotron terahertz (THz) far-infrared (FarIR) vibrational spectroscopy was further employed to monitor the bonding evolution during the formation of a_gZIF-62_CN-25 (Fig. 3g, h). Upon heating from 25 to 293 °C, Zn-related vibration remains largely stable in the raw spectra, suggesting the relative persistence of Zn-centered local environments during thermal treatment. The 400-640 cm^{-1} region remains largely invariant upon heating, with only minor changes near ~630 cm^{-1}. But there is still same phenomenon as ex-situ THz/FarIR result, showing a peak splitting around 270 cm^{-1} and the peak broadening around 630 cm^{-1}. A detailed analysis with second-derivative spectra (Fig. 3h, S12) gives more information: in the 200-400 cm^{-1} region, an emergence of a new mode ca. 300 cm^{-1} displaying clearly as heated to 300 °C is consistent with the new Zn-N bond, accompanied by a slight frequency shift and intensity redistribution. The correlated shifts in Zn-centered collective modes reveal that strong interfacial interactions are established during the thermally induced reorganization process. In the 600-700 cm^{-1} region, the processed spectra (Fig. S12) indicate the corresponding molecular structure undergoes strong intense frequency vibrations during the re-coordination process. These vibrations can be attributed to in-plane and out-of-plane aromatic ring deformation modes of imidazolate[34], which are further associated with π-π interactions between the imidazolate-based linkers and the heptazine units of g-C_3N_4. These results suggest that local Zn–N re-coordination between Zn centers and Lewis-basic nitrogen sites in g-C_3N_4 modifies the Zn-centered local geometry and induces interfacial structural distortion,

View Article Online
DOI: 10.1039/D6SC00077K

rather than forming a perfectly pristine coordination environment.

Fourier transform infrared spectroscopy (FTIR) was employed to investigate the stretching vibrations of chemical bonds and functional groups in a_gZIF-62_CN-x composites before and after sintering (Fig, 4a, S13). The spectra of a_gZIF-62_CN-x composites exhibit characteristic vibrational features from both g-C_3N_4 and a_gZIF-62. Specifically, the C-N stretching vibration from ZIF-62 appears at ~1100 cm^{-1}, which can also be observed in a_gZIF-62 and a_gZIF-62_CN-x composites. In addition, from composites' spectra, the broad absorption band in the range of 3250-2970 cm^{-1} can be assigned to the N-H stretching vibrations of terminal -NH_2 /-NH groups in g-C_3N_4[35], consistent with the spectrum of pristine g-C_3N_4 (Fig. S13). These results confirm the coexistence of both structural motifs within the composites. In the FTIR spectra of the a_gZIF-62_CN-25 and a_gZIF-62_CN-40 glass composites, a remarkable absorption band appears at ~1033 cm^{-1} which is absent in pristine a_gZIF-62. This new band is assigned to a C-N stretching vibration[36–38] associated with interfacial interactions between ZIF-62 and g-C_3N_4. The emergence of this new vibrational peak indicates that the composite formation process induces local structural rearrangement, changing the C-N bonding environment and potentially forming new coordination states. To further corroborate these findings, X-ray photoelectron spectroscopy (XPS) was performed on (Fig. S14) ZIF-62, a_gZIF-62, and a_gZIF-62_CN-25. All samples appear to have corresponding 2p 3/2 and 2p 1/2 of Zn peaks, respectively. However, the Zn 2p binding energies in the sintered samples (1045.24 eV and 1022.14eV) are shifted towards higher bonding energies relative to those in the crystalline state (1044.9eV and 1021.8eV), suggesting the indicating decreased electron density around Zn and the formation of stronger Zn–N interfacial coordination bonds[39].

The improved processing integrity of the composite is first evidenced at the macroscopic level. As shown in Fig. S18, pure a_gZIF-62 pellets consistently develop visible cracks upon cooling from the melt, whereas a_gZIF-62_CN-25 pellets prepared under identical conditions remain macroscopically intact. In addition, to demonstrate the feasibility of employing the composite materials as self-supporting devices, their mechanical properties were further evaluated. Nanoindentation was employed to compare the local mechanical response of the pellets, including elastic stiffness and resistance to plastic deformation (Fig. 4b). Measurements were performed using a Berkovich diamond tip under load-control mode (maximum load 1 mN; loading-hold-unloading sequence of 10 s, 5 s, and 15 s, respectively). As shown in Fig. 4b, both the hardness (H) and elastic modulus (E) of the a_gZIF-62_CN-x composites depend strongly on the g-C_3N_4 loading. Pristine a_gZIF-62 exhibited an E of 6.29 ± 0.26 GPa and H of 0.76 ± 0.06 GPa, inline with the reported values[40,41]. The incorporation of 10 wt% g-C_3N_4 produced a modest increase in both parameters, while at 25 wt% g-C_3N_4 resulted in the highest E (8.18 ± 0.33 GPa) and H (1.1 ± 0.03 GPa), demonstrating an optimal reinforcement effect. Carbon nitride is an exceptionally stiff and hard material, with bulk modulus and hardness reported to approach those of diamond[42]. Thus, integrating g-C_3N_4 into a_gZIF-62 is expected

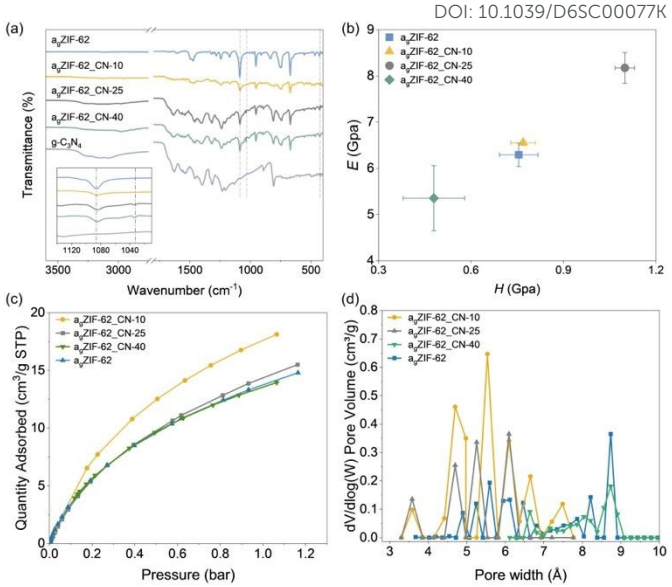

Fig. 4 Physicochemical properties of glass composites. (a) FTIR spectra of g-C_3N_4, a_gZIF-62, a_gZIF-62_CN-10, a_gZIF-62_CN-25, a_gZIF-62_CN-40 (b) Hardness-Modulus correlation of glass composite pellets. (c) CO_2 adsorption isotherm curves and (d) pore size distribution at 273K of a_gZIF-62, a_gZIF-62_CN-10, a_gZIF-62_CN-25, a_gZIF-62_CN-40.

to enhance both E and H. Moreover, π-π stacking interactions between the conjugated heptazine units of g-C_3N_4 and the imidazolate-based linkers of ZIF-62 likely enhance interfacial load transfer and improve membrane formability, contributing to the effective reinforcement. Additionally, the relatively processable and loosely stacked layered structure of g-C_3N_4 acts as a stress-buffering phase, improving processing tolerance during materials handling and shaping [43]. However, excessive g-C_3N_4 addition leads to a marked decrease in both E and H at 40 wt% loading. This deterioration is unlikely to arise from nanosheet agglomeration alone but may also reflect a loading-dependent wetting/compatibility limitation during melt processing. g-C_3N_4 contains abundant nitrogen sites and terminal –NH/–NH_2 groups, giving it a relatively polar surface, whereas the imidazolate-rich ZIF-62 glass matrix is comparatively less polar. At moderate loading, interfacial interactions between g-C_3N_4 and ZIF-62 can promote effective reinforcement. However, when the g-C_3N_4 content becomes excessive, the molten ZIF-62 phase may be insufficient to fully wet and confine the increasing nanosheet surface area, resulting in nanosheet self-aggregation, structural heterogeneity, and inefficient load transfer. These effects collectively account for the reduced E and H observed at 40 wt% loading. To further probe the effect of g-C_3N_4 incorporation on the melt and glass-forming dynamics[16], DSC-based fragility analysis was additionally performed (Fig. S23). The fragility index (m) decreases slightly from 23.18 for pristine a_gZIF-62 to 22.01 for a_gZIF-62_CN-25, indicating moderately suppressed structural relaxation dynamics and slightly stronger glass-forming behaviour after g-C_3N_4 incorporation.

View Article Online
DOI: 10.1039/D6SC00977K

To evaluate the evolution of microstructures and accessible microporosity, gas adsorption-desorption isotherm tests were carried out on the composites before and after sintering. Previous gas adsorption studies on ZIF glass materials demonstrated that when N_2 was used as a probe gas, it could not access the micropores of a_gZIF-62 due to kinetic limitations[14]. Therefore, CO_2 was employed as the probe gas to collect genuine Burnauer-Emmett-Teller (BET) surface areas for these samples (Fig. S15), where CO_2 adsorption at 195K occurs under sub-critical conditions, enabling efficient micropore filling which can be reliably measured up to P/ P_0= 1 with more accurate estimation of micropore volumes. The BET surface area of a_gZIF-62_CN-25 is 115.2 m^2 g^{-1}, compared with 134.4 m^2 g^{-1} for a_gZIF-62. Notably, the composite shows a narrower hysteresis, indicating lower desorption barriers or a more readily recoverable pore network[44]. In addition, CO_2 adsorption at 273K was applied to analyze addition isotherms and pore size distributions with NLDFT model (Fig. 4c-d) under conditions show a pronounced population of ultramicropores (~3.5-6 Å) in a_gZIF-62_CN-10 and a_gZIF-62_CN-25, consistent with its higher CO_2 uptake. With increasing g-C_3N_4 loading, the overall PSD intensity decreases and shifts slightly toward larger pores (Fig. 4d). Pure a_gZIF-62 displays only a weak contribution in the same range which was caused by pores collapse during the melting quenching process. The isosteric heat of CO_2 adsorption (Q_{st}), obtained from dual-temperature isotherms under 273 and 298 K, via the Clausius-Clapeyron approach (Fig. S17)[45], further corroborates this result. a_gZIF-62_CN-25 exhibits a higher Q_{st} at low coverage than a_gZIF-62, evidencing stronger CO_2 surface interactions in the composite. With increasing uptake, Q⍰⍰ for both samples converges to 30 kJ mol^{-1} at 7.45 mg g^{-1}, consistent with saturation of the strongest interfacial sites followed by filling of more uniform and weaker sites[46–49]. Therefore, we found that at low temperature, the pure glass engages in stronger site-specific interactions under diffusion-limited conditions, whereas near ambient temperature the interfacial

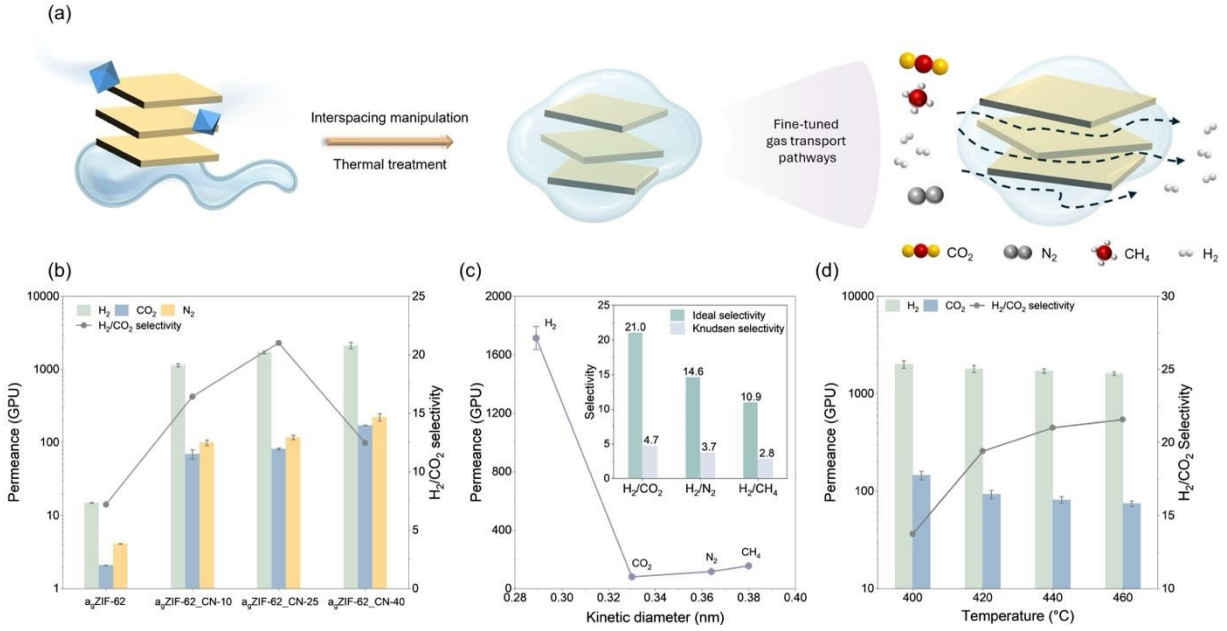

Fig. 5 Gas permeation studies. (a) Schematic illustration of interlayer spacing manipulation and gas separation mechanism of a_gZIF-62_CN-x composites. Single gas permeance test at 30°C for (b) a_gZIF-62_CN-x CGC treated under 440°C, (c) a_gZIF-62_CN-25 CGC obtained under 440°C, (d) a_gZIF-62_CN-25 CGC under different temperature annealing.

more relevant to practical gas separation[21]. Although both isotherms datasets are discussed in terms of relative pressure, the absolute saturation pressure P_0 differs at 195K P_0 ≈ 1 bar, whereas at 273K P_0 ≈ 35 bar, leading to different thermodynamic driving forces and transport behavior. At a relative pressure of P/P_0 = 0.035, a_gZIF-62_CN-10 shows the highest CO_2 adsorption capacity of 18.12 cm^3/g STP. With further increasing of g-C_3N_4 (25 and 40 wt%), the gas uptake capacity decreases, approaching the value of pristine a_gZIF-62. This decline is attributed primarily to a compositional dilution of the pore-forming glassy phase rather than pore blocking, because g-C_3N_4 itself exhibits very low CO_2 uptake at 273 K (Fig. S16) and contributes minimally to accessible microporosity. Based on NLDFT (CO_2 273 K), the pore-size distributions (PSD) sites and improved accessibility in a_gZIF-62_CN-25 dominate.

Owing to its good processability and mechanical robustness, the absence of significant microscopic defects, and the presence of accessible micropores, this composite was employed to fabricate separation membranes via a hot-pressing approach. This platform enables us to systematically investigate how modifications in the stacking of the two-dimensional g-C_3N_4 sheets influence the gas transport and separation performance of the resulting composite membranes. The single gas permeation performance was systematically evaluated at 30 °C (Fig. 5, Table S2). Because the present membrane is a thick self-supporting MOF glass–2D nanosheet composite rather than a homogeneous dense film, macroscopic thickness-normalized

View Article Online DOI: 10.1039/D6SC00977K

permeability values should be interpreted with caution. The gas separation performance is therefore discussed mainly in terms of measured permeance and selectivity, together with comparison to related self-supported MOF glass and porous framework-based membranes. For pristine a_gZIF-62, the H_2 permeance was limited to 14.9 GPU with a low ideal H_2/CO_2 selectivity, reflecting the intrinsic transport restriction of the dense and disordered glassy network nature (Fig. 5a). Upon incorporation of g-C_3N_4 nanosheets, the permeance of all tested gases increased significantly, with H_2 showing the most pronounced enhancement. Among all compositions in Fig. 5b, a_gZIF-62_CN-25 shows the best performance, achieving both high H_2 permeance (1716 GPU) and H_2/CO_2 selectivity (21). Higher loading (40 wt%) increases H_2 permeance to 2133.5 GPU but sacrifices H_2/CO_2 selectivity (12.5) due to partial nanosheet aggregation and the formation of non-selective pathways. Thus, a_gZIF-62_CN-25 represents an optimal balance between interfacial compatibility, nanosheet dispersion, and molecular sieving. The single-gas permeance trend reflects a strong size-sieving effect (Fig. 5c), where H_2 diffuses quickly whereas CO_2 shows a sharp reduction in flux, followed by a plateau for N_2 and CH_4. The tightened interlayer spacing (ca. 0.32 nm) falls between the kinetic diameters of H_2 (0.289 nm) and CO_2 (0.33 nm), enabling facile H_2 diffusion while imposing an orientation-dependent barrier for CO_2[30,50]. It should be noted that this does not imply that gas transport occurs exclusively through the g-C_3N_4 interlayers. The CO_2 adsorption-derived pore-size distribution reflects accessible pore cavities and free-volume elements, whereas membrane sieving is governed by the effective aperture and connectivity of transport channels. Correspondingly, the measured a_gZIF-62_CN-25 ideal selectivity for H_2/CO_2 (21), H_2/N_2 (14.6), and H_2/CH_4 (10.9) substantially exceed their respective Knudsen values (4.7, 3.7, and 2.8). Fig. S21 compares the H_2/CO_2 separation performance of the a_gZIF-62_CN-x membranes with MOF, COF, 2D material and porous framework-based membranes reported in the literature at room temperature. Despite being a self-supporting membrane with a thickness of several hundred micrometres, a_gZIF-62_CN-25 exhibits high H_2 permeance while maintaining considerable H_2/CO_2 selectivity, placing its overall performance within the upper range of emerging porous framework-derived functional membranes.

To further distinguish diffusion-related transport trends across the membrane series, apparent diffusivity values were obtained from pure-gas time-lag measurements and summarized in Table S4. It should be noted that these values are used only for internal comparison among membranes tested under the same conditions, rather than as intrinsic material constants, because the thick self-supporting composite pellets may not behave as homogeneous dense membrane phases. Despite this limitation, H_2 exhibits a higher apparent diffusivity than CO_2 across the membrane series, supporting preferential H_2 diffusion through confined microporous or interfacial pathways. Therefore, the enhanced H_2/CO_2 separation performance is reasonably attributed to the cooperative effects of introduced interlayer spacing, improved pore and interlayer connectivity, and faster H_2 diffusion through the composite transport network.

To assess the separation performance under more practical conditions, mixed-gas H_2/CO_2 permeation tests were further conducted using a Wicke–Kallenbach apparatus under steady-state conditions in Fig. S19. The mixed-gas separation factor remained close to the ideal selectivity with only a slight decrease, indicating that competitive CO_2 adsorption does not significantly disrupt the H_2 selective transport pathway within the rigid MOF glass composite structure. In addition, long-term permeation measurements over ~90 h (Fig. S20) further demonstrate that the a_gZIF-62_CN-25 membrane maintains stable H_2 permeance and H_2/CO_2 selectivity with only minor fluctuations, suggesting that the incorporation of g-C_3N_4 helps suppress rapid structural relaxation of the glass matrix and stabilizes the composite transport network during operation.

To further probe the role of thermal treatment and change of interlayer space, a_gZIF-62_CN-25 membranes were annealed at different temperatures between 400 and 460 °C (Fig. 5d). H_2 permeance remained above 1000 GPU across all samples, but showed a slight decrease compared with the increase of treated temperature, aligning well with the change of interlayer space. In contrast, CO_2 permeance decreased more noticeably with increasing treatment temperature, leading to a modest but consistent improvement in H_2/CO_2 selectivity. The highest H_2/CO_2 selectivity of 23.4 was achieved after annealing at 460 °C, indicating that high-temperature treatment reinforces Zn-N coordination and π-π interactions. These synergistic interfacial interactions between g-C_3N_4 and the ZIF-62 glass matrix enhance interlayer confinement and promote the formation of continuous, well-connected transport channels, facilitating rapid H_2 diffusion and superior molecular sieving. Overall, these results demonstrate that nanoscale incorporation combined with thermal treatment can precisely tune interfacial coordination and interlayer spacing, enabling hybrid glass membranes with both high H_2 permeance and elevated H_2/CO_2 selectivity. More broadly, this strategy establishes a general structure-performance paradigm for designing multifunctional hybrid materials, where interfacial and nanoscale control can be leveraged to optimise transport, mechanical, and functional properties.

Conclusions

We have demonstrated in this work that the integration of g-C_3N_4 nanosheets into ZIF-62 glass through high temperature sintering enables precise control and stabilization of interlayer spacing, formed via strong and effective interfacial interactions. The incorporation of nanosheets also enhances processability and mechanical integrity. Future work should include direct quantification of fracture toughness using single-edge notched beam testing or micro-cantilever bending to better understand the bulk crack resistance of these composites. A more comprehensive rheological analysis of the composite melt is also identified as an important direction for future study. The resultant hybrid glass membranes show significantly improved membrane hydrogen separation performance. Beyond gas separation, this approach provides a versatile platform for designing hybrid amorphous materials with tunable

microstructure and interface properties. It could be further extended to other two-dimensional or layered materials, opening opportunities for nanosheet materials assembly towards applications like selective separation, catalysis, ion transport, and beyond.

Author contributions

J. H. and J. Y. conceived this research and contributed to draft and edited the manuscript. S. Z., B. C. and W. L. conducted testing experiments and collected the data. W. H. and M. Y. carried out data analysis. Zhonghao Xu prepared the figures and visualization materials. M. C., S. Y. and M. L. provided training on characterization instruments. W. L., X. Z., V. C., J. H. and R. L. provided instrumentation access and supervised the project with critical feedback. All authors have given approval to the final version of the manuscript.

Conflicts of interest

There are no conflicts to declare.

Data availability

All of the necessary data have been included in the main text and the ESI.†

Acknowledgements

The authors acknowledge the funding support from the Australian Research Council (ARC) (FT210100589, and DP230101901). This research was conducted by the ARC Centre of Excellence for Green Electrochemical Transformation of Carbon Dioxide (CE230100017) and funded by the Australian Government. This research acknowledges the Natural Science Research Project of Anhui Provincial Education Department (2022AH030135). This research was undertaken on the THz, PD and X-ray Absorption beamlines at the Australian Synchrotron, part of ANSTO.

Notes and references

1 H.-N. Li, Z.-Y. Sun, Z.-J. Yu, K. Man, C. Zhang and Z.-K. Xu, *Nat Commun*, 2025, **16**, 8199.
2 P. Motamed, R. S. Othman, M. Golriz, M. Naqvi, A. Afshar Taromi and H. A. Khonakdar, *ChemistrySelect*, 2025, **10**, e03697.
3 C. Ji, H. Shao, Y. Pu, H. Zhang, H. Li, W.-H. Li, N. Zhu, W. Zhao, D. Jiang and D. Zhao, *Advanced Materials*, **n/a**, e13499.
4 Y. Zhang, B. H. Yin, L. Huang, L. Ding, S. Lei, S. G. Telfer, J. Caro and H. Wang, *Progress in Materials Science*, 2025, **151**, 101432.
5 Y. Feng, W. Yan, Z. Kang, X. Zou, W. Fan, Y. Jiang, L. Fan, R. Wang and D. Sun, *Chemical Engineering Journal*, 2023, **465**, 142873.
6 G. Liu, Y. Guo, C. Chen, Y. Lu, G. Chen, G. Liu, Y. Han, W. Jin and N. Xu, *Nat. Mater.*, 2023, **22**, 769–776.
7 S. Li, C. Ma, J. Hou, S. Yu, A. Chen, J. Du, P. A. Chater, D. S. Keeble, Z. Qiao, C. Zhong, D. A. Keen, Y. Liu and T. D. Bennett, *Nat Commun*, 2025, **16**, 1622.
8 D. Li, Z. Yang, L. Yang, C. Ma, M. Ye, Y. Sun, Z. Qiao and A. Chen, *Journal of Membrane Science*, 2024, **695**, 122492.
9 M. Kim, H.-S. Lee, D.-H. Seo, S. J. Cho, E. Jeon and H. R. Moon, *Nat Commun*, 2024, **15**, 1174.
10 Z. Chen, Z. Xu, X. Zhong, Y. Chen, S. Yang, Y. Feng, P. Zhang, Y. Li, M. Xue and X. Chen, *Advanced Materials*, 2025, e12654.
11 J. Li, J. Wang, Q. Li, M. Zhang, J. Li, C. Sun, S. Yuan, X. Feng and B. Wang, *Angewandte Chemie International Edition*, 2021, **60**, 21304–21309.
12 A. E. Khudozhitkov, N. Ogiwara, M. Donoshita, H. Kobayashi, A. G. Stepanov, D. I. Kolokolov and H. Kitagawa, *J. Am. Chem. Soc.*, 2024, **146**, 12950–12957.
13 T. To, S. S. Sørensen, M. Stepniewska, A. Qiao, L. R. Jensen, M. Bauchy, Y. Yue and M. M. Smedskjaer, *Nat Commun*, 2020, **11**, 2593.
14 L. Frentzel-Beyme, P. Kolodzeiski, J.-B. Weiß, A. Schneemann and S. Henke, *Nat Commun*, 2022, **13**, 7750.
15 J. C. Mauro, Y. Yue, A. J. Ellison, P. K. Gupta and D. C. Allan, *Proc. Natl. Acad. Sci. U.S.A.*, 2009, **106**, 19780–19784.
16 A. Qiao, T. D. Bennett, H. Tao, A. Krajnc, G. Mali, C. M. Doherty, A. W. Thornton, J. C. Mauro, G. N. Greaves and Y. Yue, *Sci. Adv.*, 2018, **4**, eaao6827.
17 O. Smirnova, R. Sajzew, S. J. Finkelmeyer, T. Asadov, S. Chattopadhyay, T. Wieduwilt, A. Reupert, M. Presselt, A. Knebel and L. Wondraczek, *Nat Commun*, 2024, **15**, 5079.
18 O. N. Senkov, *Phys. Rev. B*, 2007, **76**, 104202.
19 T. D. Bennett, J.-C. Tan, Y. Yue, E. Baxter, C. Ducati, N. J. Terrill, H. H.-M. Yeung, Z. Zhou, W. Chen, S. Henke, A. K. Cheetham and G. N. Greaves, *Nat Commun*, 2015, **6**, 8079.
20 T. D. Bennett, S. Horike, J. C. Mauro, M. M. Smedskjaer and L. Wondraczek, *Nat. Chem.*, 2024, **16**, 1755–1766.
21 L. N. McHugh and T. D. Bennett, *J. Mater. Chem. A*, 2022, **10**, 19552–19559.
22 F. Cui, V. García-López, Z. Wang, Z. Luo, D. He, X. Feng, R. Dong and X. Wang, *Chem. Rev.*, 2025, **125**, 445–520.
23 Y. Ren and Y. Xu, *Chem. Soc. Rev.*, 2024, **53**, 1823–1869.
24 T. Bao, X. Li, S. Li, H. Rao, X. Men, P. She and J. Qin, *Nano Materials Science*, 2025, **7**, 145–168.
25 F. K. Kessler, Y. Zheng, D. Schwarz, C. Merschjann, W. Schnick, X. Wang and M. J. Bojdys, *Nat Rev Mater*, 2017, **2**, 17030.
26 C.-C. Wang, X.-H. Yi and P. Wang, *Applied Catalysis B: Environmental*, 2019, **247**, 24–48.
27 Y. Liu, D. Luo, Y. Wang, X. Ma, S. Shen, B. Bai and C. Sun, *Nano Lett.*, 2025, **25**, 14582–14590.
28 Y. Wang, T. Lian, N. V. Tarakina, J. Yuan and M. Antonietti, *Nat Commun*, 2022, **13**, 7339.
29 X. Li, W. Huang, A. Krajnc, Y. Yang, A. Shukla, J. Lee, I. Martens, B. Chan, D. Appadoo, P. Chen, X. Weng, J. A. Steele, Q. Sun, G. Mali, R. Lin, N. Bedford, V. Chen, K. Cheetham, L. H. G. Tizei, S. M. Collins, L. Wang and J. Hou, .
30 Y. Zhou, Y. Wu, H. Wu, J. Xue, L. Ding, R. Wang and H. Wang, *Nat Commun*, 2022, **13**, 5852.
31 H. Wang, D. Chen, X. An, Y. Zhang, S. Sun, Y. Tian, Z. Zhang, A. Wang, J. Liu, M. Song, S. P. Ringer, T. Zhu and X. Liao, *Science Advances*, 2021, **7**, eabe3105.
32 W. Huang, B. Chan, Y. Yang, P. Chen, J. Wang, L. Casey, C. Atzori, T. Schulli, O. Mathon, H. G. Hackbarth, N. M. Bedford, D. Appadoo, X. Li, T. Lin, R. Lin, J. Lee, Z. Wang, V. Chen, A. K. Cheetham, L. Wang and J. Hou, *J. Am. Chem. Soc.*, 2025, **147**, 3195–3205.

View Article Online
DOI: 10.1039/D6SC00077K

33 W. Huang, W. Xue, P. Chen, Z. Wang, R. Lin, S. Zhao, S. Yu, Y. Chen, X. Zha, D. Appadoo, T. Tian, V. Chen, S. Henke, A. K. Cheetham, L. Wang and J. Hou, *Angewandte Chemie*, 2025, **137**, e202506570.
34 J. Hou, M. L. Ríos Gómez, A. Krajnc, A. McCaul, S. Li, A. M. Bumstead, A. F. Sapnik, Z. Deng, R. Lin, P. A. Chater, D. S. Keeble, D. A. Keen, D. Appadoo, B. Chan, V. Chen, G. Mali and T. D. Bennett, *J. Am. Chem. Soc.*, 2020, **142**, 3880–3890.
35 H. Liu, B. Yang, G. Liao, B. Huang, J. Li, R. D. Rodriguez and X. Jia, *Nat Commun*, 2025, **16**, 5909.
36 K. S. Fathima and K. Anitha, Bhubaneswar, Odisha, India, 2017, p. 100016.
37 Z. Öztürk, M. Filez and B. M. Weckhuysen, *Chemistry – A European Journal*, 2017, **23**, 10915–10924.
38 Y. Hu, Z. Liu, J. Xu, Y. Huang and Y. Song, *J. Am. Chem. Soc.*, 2013, **135**, 9287–9290.
39 R. Lin, J. Hou, M. Li, Z. Wang, L. Ge, S. Li, S. Smart, Z. Zhu, T. D. Bennett and V. Chen, *Chem. Commun.*, 2020, **56**, 3609–3612.
40 T. D. Bennett, Y. Yue, P. Li, A. Qiao, H. Tao, N. G. Greaves, T. Richards, G. I. Lampronti, S. A. T. Redfern, F. Blanc, O. K. Farha, J. T. Hupp, A. K. Cheetham and D. A. Keen, *J. Am. Chem. Soc.*, 2016, **138**, 3484–3492.
41 R. Lin, M. Chai, Y. Zhou, V. Chen, T. D. Bennett and J. Hou, *Chem. Soc. Rev.*, 2023, **52**, 4149–4172.
42 H. Dong, A. R. Oganov, Q. Zhu and G.-R. Qian, *Sci Rep*, 2015, **5**, 9870.
43 L. Chen and J. Song, *Advanced Functional Materials*, 2017, **27**, 1702695.
44 S. Yang, X. Lin, W. Lewis, M. Suyetin, E. Bichoutskaia, J. E. Parker, C. C. Tang, D. R. Allan, P. J. Rizkallah, P. Hubberstey, N. R. Champness, K. Mark Thomas, A. J. Blake and M. Schröder, *Nature Mater*, 2012, **11**, 710–716.
45 M. Yin, L. Wang and S. Tang, *ACS Catal.*, 2023, **13**, 13021–13033.
46 J. Seo, R. Matsuda, H. Sakamoto, C. Bonneau and S. Kitagawa, *J. Am. Chem. Soc.*, 2009, **131**, 12792–12800.
47 F. Li, X. Yue, Y. Liao, L. Qiao, K. Lv and Q. Xiang, *Nat Commun*, 2023, **14**, 3901.
48 Z. Zhang, Y. Chen, K. Chai, C. Kang, S. B. Peh, H. Li, J. Ren, X. Shi, X. Han, C. Dejoie, S. J. Day, S. Yang and D. Zhao, *Nat Commun*, 2023, **14**, 3789.
49 G. Férey and C. Serre, *Chem. Soc. Rev.*, 2009, **38**, 1380–1399.
50 R. Wang, J. Qian, X. Chen, Z.-X. Low, Y. Chen, H. Ma, H.-A. Wu, C. M. Doherty, D. Acharya, Z. Xie, M. R. Hill, W. Shen, F. Wang and H. Wang, *Nat Commun*, 2023, **14**, 2161.

View Article Online
DOI: 10.1039/D6SC00077K

The data supporting this article have been included as part of the Supplementary Information.